RESEARCH ARTICLE

Key Points:
- Radar-based velocity allows for detection of meteotsunami-inducing front
- Wave reflection, focusing, and edge waves led to meteotsunami conditions
- Enclosed basins can induce temporal lags between storm front and wave response

Supporting Information:
- Supporting Information S1
- Movie S1
- Movie S2
- Movie S3

Correspondence to:
E. J. Anderson,
eric.j.anderson@noaa.gov

Reconstruction of a meteotsunami in Lake Erie on 27 May 2012: Roles of atmospheric conditions on hydrodynamic response in enclosed basins

Eric J. Anderson[1], Adam J. Bechle[2], Chin H. Wu[2], David J. Schwab[3], Greg E. Mann[4], and Kirk A. Lombardy[5]

[1]Great Lakes Environmental Research Laboratory, National Oceanic and Atmospheric Administration, Ann Arbor, Michigan, USA, [2]Department of Civil and Environmental Engineering, University of Wisconsin-Madison, Madison, Wisconsin, USA, [3]Water Center, University of Michigan, Ann Arbor, Michigan, USA, [4]National Weather Service, Weather Forecast Office, National Oceanic and Atmospheric Administration, White Lake, Michigan, USA, [5]National Weather Service, Weather Forecast Office, National Oceanic and Atmospheric Administration, Cleveland, Ohio, USA

Abstract On 27 May 2012, atmospheric conditions gave rise to two convective systems that generated a series of waves in the meteotsunami band on Lake Erie. The resulting waves swept three swimmers a 0.5 mi offshore, inundated a marina, and may have led to a capsized boat along the southern shoreline. Analysis of radial velocities from a nearby radar tower in combination with coastal meteorological observation indicates that the convective systems produced a series of outflow bands that were the likely atmospheric cause of the meteotsunami. In order to explain the processes that led to meteotsunami generation, we model the hydrodynamic response to three meteorological forcing scenarios: (i) the reconstructed atmospheric disturbance from radar analysis, (ii) simulated conditions from a high-resolution weather model, and (iii) interpolated meteorological conditions from the NOAA Great Lakes Coastal Forecasting System. The results reveal that the convective systems generated a series of waves incident to the southern shore of the lake that reflected toward the northern shoreline and reflected again to the southern shore, resulting in spatial wave focusing and edge wave formation that combined to impact recreational users near Cleveland, OH. This study illustrates the effects of meteotsunami development in an enclosed basin, including wave reflection, focusing, and edge wave formation as well as temporal lags between the causative atmospheric conditions and arrival of dangerous wave conditions. As a result, the ability to detect these extreme storms and predict the hydrodynamic response is crucial to reducing risk and building resilient coastal communities.

1. Introduction

Meteotsunami events have been documented in several countries around the world, causing destructive impacts to coastal communities while being difficult to forecast [*Candela et al.*, 1999; *Jansa et al.*, 2007; *Vilibić et al.*, 2008; *Dragani et al.*, 2009; *Šepić et al.*, 2009; *Thomson et al.*, 2009; *Asano et al.*, 2012; *Pasquet and Vilibić*, 2013; *Vilibić et al.*, 2014]. Meteotsunamis are waves with periods between 2 h and 2 min that are generated by an atmospheric disturbance and behave more like seismic tsunami waves than storm surge or seiche events [*Monserrat et al.*, 2006]. Meteotsunami-generating atmospheric disturbances most commonly entail a sharp gradient in pressure [*Vilibić*, 2005; *Orlić et al.*, 2010], though wind stress has also been shown to be of significant importance to meteotsunami generation in the Great Lakes [*As-Salek and Schwab*, 2004; *Bechle and Wu*, 2014; *Šepić and Rabinovich*, 2014]. Investigations in the Great Lakes have also raised the issue of dangers posed by meteotsunamis in enclosed basins due to the reflection and interaction of meteotsunami waves, in which the destructive waves can arrive several hours after the atmospheric disturbance has passed [*Ewing et al.*, 1954; *Bechle and Wu*, 2014]. This disassociation in time and space between the atmospheric disturbance and resultant meteotsunami wave can pose a significant threat to lake users. These events justify the need to understand and forecast meteotsunami threat in enclosed basins.

The formation of a meteotsunami involves three processes: wave generation, propagation resonance, and local response [*Monserrat et al.*, 2006]. First, an atmospheric disturbance in the form of a squall line, derecho, atmospheric gravity waves, or other similar weather system generates an initial water level displacement in the open

water, termed a meteorological wave [*Rabinovich*, 2009]. These waves travel in the form of long waves, governed by the shallow water wave speed, or edge waves, which are coastally trapped by topographic refraction and are governed by an edge wave dispersion relation [*Ursell*, 1952]. Interaction between these waves and the atmospheric disturbance dictates the generation and growth of the meteotsunami waves, where the primary drivers are pressure, wind stress, and propagation speed [*Vilibić*, 2008]. Second, propagation resonance occurs when the atmospheric disturbance and the water wave travel at a similar speed, which allows atmospheric energy to be constantly fed into the water wave to increase amplitude by up to an order of magnitude [*Donn and Balachandran*, 1969]. Finally, meteotsunamis can be enhanced by local mechanisms as the waves approach the coast. Wave height can be amplified by up to 2 orders of magnitude through a combination of shoaling, shelf resonance, spatiotemporal focusing, and harbor resonance [*Vilibić*, 2005]. While the processes behind many of these mechanisms are understood, the specific response to transient meteotsunami oscillations is not clear, particularly for the interactions of long waves and edge waves in enclosed basins.

The Great Lakes have a long recorded history of events that embody the characteristics associated with meteotsunamis in enclosed basins. However, meteotsunami terminology was relatively unmentioned until recently, and in most cases, these incidents were originally described as storm surges or tidal waves [*Ewing et al.*, 1954]. Most notably was the formation of a 3 m meteotsunami wave in Lake Michigan in 1954, in which several fishermen were swept off of a pier in Chicago, killing seven [*Bechle and Wu*, 2014]. Lake Erie, the smallest and shallowest of the Great Lakes, has also experienced several destructive meteotsunami events. On the morning of 23 June 1882, a 3 m wave struck Cleveland, which drowned one person, grounded barges, and extinguished fires at a steel rolling mill [*Cleveland Plain Dealer*, 1882]. On the evening of 12 April 1912, a large wave at Ashtabula, OH, broke a steamship loose from her moorings, sending the vessel into a collision with a freighter [*New York Times*, 1912]. The most tragic Lake Erie meteotsunami occurred on 31 May 1942, when a 4.5 m wave struck the coast near Cleveland, leading to capsized boats and drowning seven fishermen who were swept into the lake [*Toledo Blade*, 1942]. However, due to the fine-scale spatial and temporal nature of these storms and the resultant meteotsunamis, detection, measurement, and characterization of meteotsunamis in the Great Lakes are extremely difficult and rare, even if they occur more often than is implied by historical records.

In this paper, we aim to investigate the origin of a recent meteotsunami event in Lake Erie on 27 May 2012. Meteorological observations are analyzed to identify three atmospheric disturbances that had the potential to cause the meteotsunami waves observed in water level records. A hydrodynamic model of Lake Erie is used to simulate the meteotsunami event in response to meteorological conditions from three scenarios: (i) reconstructed meteorology from observations, (ii) simulated atmospheric conditions from a high-resolution WRF model, and (iii) interpolated meteorological conditions from the Great Lakes Coastal Forecasting System (GLCFS). The results of the hydrodynamic simulation are analyzed to determine the cause of the meteotsunami waves. The resulting analysis gives us insight into the development of meteotsunamis in enclosed basins using modern observations and modeling techniques. Furthermore, the results presented here underscore the uniqueness of meteotsunami or extreme storm conditions in an enclosed basin and the dangers posed by wave reflection and energy focusing as well as the temporal differences between the atmospheric forcing conditions and the meteotsunami response.

2. Meteotsunami Event at Study Site

During Memorial Day weekend in 2012, recreational swimmers and boaters along the southern shoreline of Lake Erie were impacted in at least three separate events on 27 May that embodied the traits of a meteotsunami (Figure 1). In addition to being a holiday weekend, warm lake conditions were favorable for increased recreational use and thus elevated susceptibility to dangerous conditions (5.0°C above long-term average on day 150; Great Lakes Surface Environmental Analysis, GLSEA) [*Schwab et al.*, 1992, 1999]. In the afternoon of 27 May, atmospheric conditions gave rise to two mesoscale convective systems from the northwest that traveled across Lake Erie from Ontario, Canada, toward east of Cleveland, Ohio (Figure 2). At 17:30 GMT, an eyewitness east of Cleveland, OH, reported the arrival of three waves roughly 5 min apart with wave heights near 1–2 m (1.0–2.1 m; NOAA/NWS/WFO/Cleveland), which swept property off the beach (Figure 1). At 19:30 GMT near Lakewood, OH (11 km west of Cleveland), USCG reports that three people were rescued after their boat was capsized as a result of a 6 ft (1.8 m) wave. Nearly 2.5 h later and 80 km to the east at
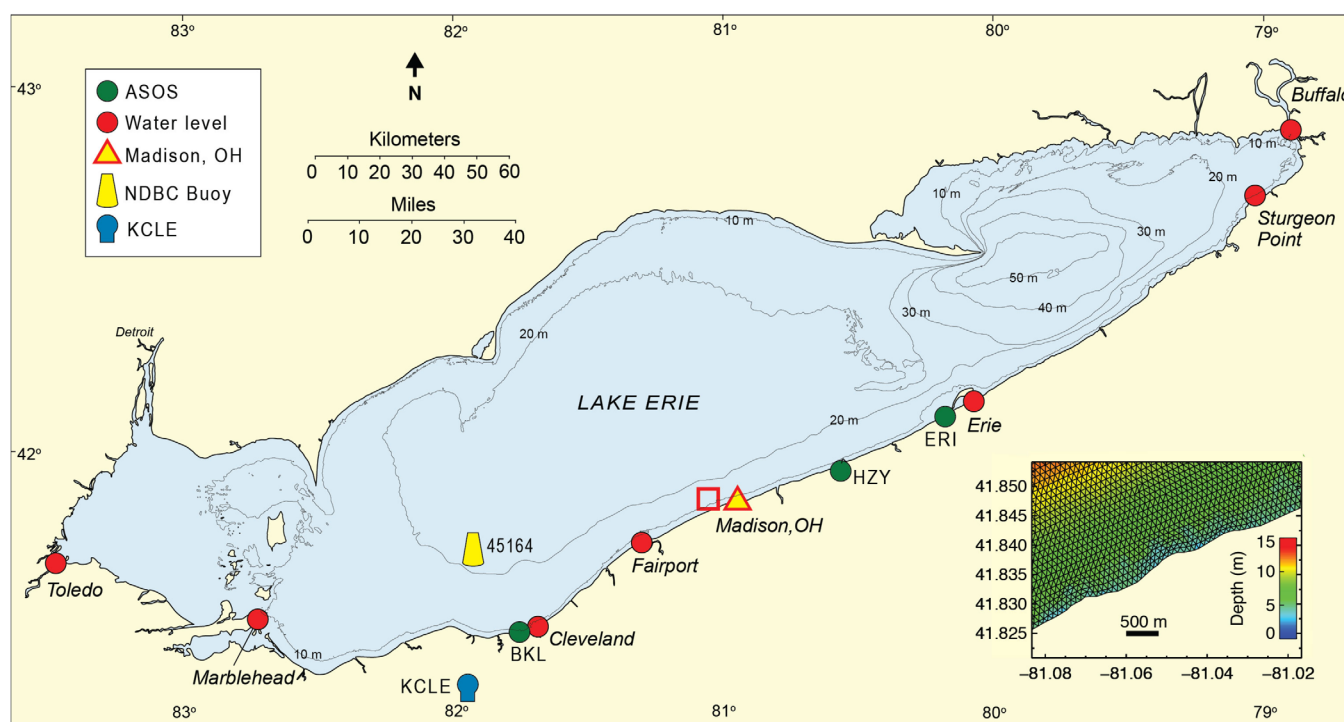
Figure 1. A map of Lake Erie with NOS/CO-OPS water level stations along the southern shore (red circles), ASOS meteorology stations (green circles) at Burke Lakefront Airport (BKL), Ashtabula, OH (HZY), and Erie, PA (ERI), an offshore buoy (NDBC 45164), radar station at KCLE (blue tower), and the impact location where three swimmers were swept into the lake (Madison, OH). Inset of hydrodynamic model mesh depicts region near Madison, OH.

22:00 GMT, after a sudden inundation of the beach, the retreating water swept three swimmers over the breakwater 0.8 km into the lake near Madison, OH (east of Fairport Harbor, OH), requiring rescue by recreational boaters in the area. Also around 22:00 GMT, the marina at Perry, OH (8 km west of Madison), became inundated, including a truck at the dock that was removing a boat from the water. Similar reports from nearby locations (up to 25 km) confirmed the rapid rise and retreat in water level, causing inundation of other nearby marinas (NOAA/NWS/WFO/Cleveland).

3. Methods

3.1. Water Level and Meteorological Data

To examine the meteotsunami event, water level, surface meteorology, and radar data are analyzed. Water level observations are obtained at 6 min intervals at seven stations along the southern shore of Lake Erie, operated by the National Ocean and Atmospheric Administration National Ocean Service. The gauge locations are illustrated by red circles in Figure 1. Wind speed, wind direction, and atmospheric pressure are obtained from the National Weather Service Automated Surface Observing System (ASOS) stations provided at 1 min intervals and shown as green circles in Figure 1. Wind speed over the lake is obtained at 15 s intervals from National Data Buoy Center (NDBC) station 45164, located approximately 20 km offshore northwest of Cleveland, illustrated as a yellow trapezoid in Figure 1. Base reflectivity and radial velocity radar data are obtained from the Cleveland, Ohio (KCLE), NEXRAD Weather Surveillance Radar-1988 Doppler (WSR-88D) station at approximately 5 min intervals (blue tower in Figure 1).

3.2. Atmospheric Reconstruction and Modeling

To characterize the overwater atmospheric conditions during the 27 May 2012 event, we use both observations and modeled atmospheric conditions. We reconstruct the observed surface meteorology with idealized atmospheric pressure and wind speed perturbations. First, a series of linear changes in atmospheric pressure and wind speed are constructed to best represent the time series of wind speed and atmospheric pressure observed at Cleveland Burke Lakefront Airport (BKL) and the wind speed at offshore buoy NDBC 45164. Second, the velocity of these surface perturbations is obtained from tracking the associated storm
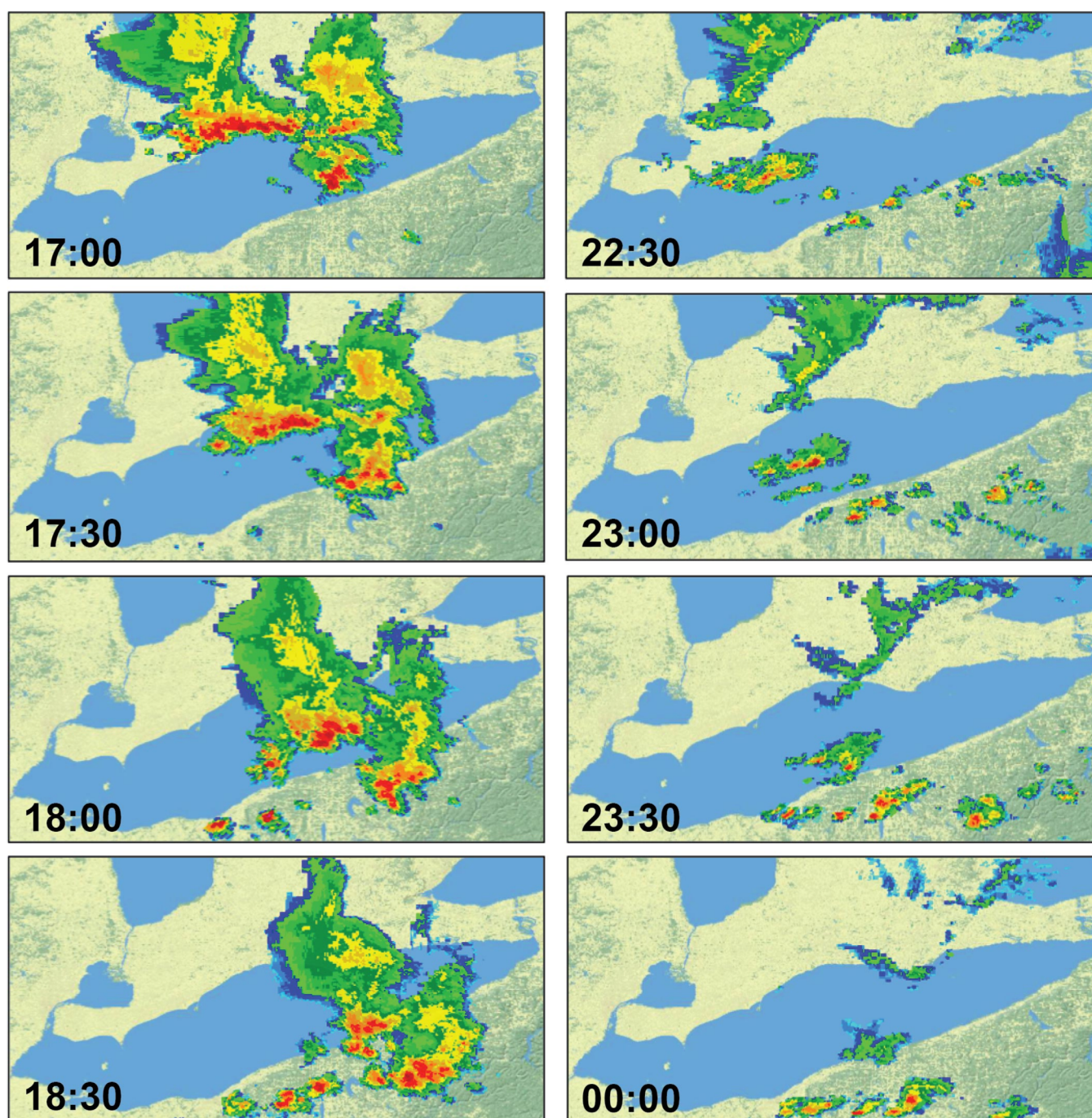
Figure 2. Doppler radar from the Cleveland radar tower (KCLE) shows the reflectivity associated with the convective systems as the pass over Lake Erie from the north on 27 May 2012 (times shown in GMT).

paths in the radar radial velocity measurements from KCLE. Third, spatial representations of the surface conditions are generated by applying the storm velocities to time series of atmospheric pressure and wind speed. Surface perturbations are assumed to be one dimensional in the direction of the storm path with uniform conditions along the outflows (perpendicular to storm direction). Finally, the spatial representations of the surface conditions are propagated at the observed storm velocities, yielding a time series of reconstructed storm-scale spatial atmospheric pressure and winds fields that closely match the observed meteorology. To fill in any gaps in the meteorological fields, interpolated atmospheric forcing conditions are prescribed by the Great Lakes Coastal Forecasting System (GLCFS) [*Schwab and Bedford*, 1994], which is

described below. Hereafter, model simulations forced with this meteorological representation will be referred to as the "reconstructed meteorology" case.

To simulate the atmospheric conditions during the meteotsunami event, we also use the Weather Research and Forecasting (WRF) model at spatial and temporal scales that mimic the next generation of operational capabilities [*Skamarock et al.*, 2008]. The WRF model leverages a regional domain covering the Great Lakes with a horizontal grid spacing of 1 km. Initial and boundary conditions are prescribed from the North American Regional Reanalysis (NARR) with an initial time of 12:00 GMT on 26 May 2012 [*Mesinger et al.*, 2006]. Lake surface temperatures are prescribed by the NOAA HIRES RTG 1/12th degree SST data set [*Thiébaux et al.*, 2003]. Simulation output is produced at 5 min intervals to ensure adequate time resolution of the fine spatial and short temporal-scale features associated with the mesoscale convective systems. Hereafter, hydrodynamic model simulations forced with this WRF output meteorological conditions will be referred to as the "WRF meteorology" case.

Finally, we employ the current operational meteorological forcing conditions used for the Great Lakes Coastal Forecasting System (GLCFS) [*Schwab and Bedford*, 1994]. The GLCFS uses a natural neighbor approach to interpolate meteorological conditions from several land-based stations that surround the lake to provide a representation of meso-alpha-scale conditions over the entire lake. However, it is noted that this approach cannot resolve fine-scale features association with these types of weather systems due to the lack of overwater observations. Hereafter, these atmospheric conditions will be referred to as the "GLCFS meteorology" case.

3.3. Hydrodynamic Modeling

In order to simulate the meteotsunami event, we model the hydrodynamic response to the atmospheric conditions as described above. Model simulations are carried out for three different atmospheric cases using (i) the reconstructed meteorology, (ii) WRF meteorology, and (iii) the GLCFS meteorology. In case i, reconstructed fields of pressure and wind stress are applied in combination with the peripheral interpolated GLCFS meteorological forcing to represent the idealized storm front over the lake. In addition, perturbations on wind stress and pressure of the reconstructed outflows are applied to test sensitivity of the hydrodynamic response to uncertainty in the reconstructed meteorology. In case ii, 1 km WRF simulations provide an evaluation of the next generation of the operational atmospheric models. The third case iii provides an assessment of the present state of operational forecasting and baseline for comparison with the reconstructed and WRF meteorology (cases i and ii).

A hydrodynamic model of Lake Erie that has been developed for the next generation of the NOAA Great Lakes Coastal Forecasting System (GLCFS) [*Schwab and Bedford*, 1994] is used to model the hydrodynamic response to the 27 May event. The model is based on the Finite Volume Coastal Ocean Model (FVCOM) [*Chen et al.*, 2003, 2006], a free-surface, primitive-equation hydrodynamic model that solves the integral equations of motion on an unstructured grid. For the two-dimensional barotropic case, the governing equations can be solved in the vertically integrated terrain-following (sigma-coordinate) form (equations (1)–(5)),

$$\frac{\partial \eta}{\partial t} + \frac{\partial (\overline{u}D)}{\partial x} + \frac{\partial (\overline{v}D)}{\partial y} = 0 \tag{1}$$

$$\frac{\partial \overline{u}D}{\partial t} + \frac{\partial \overline{u}^2 D}{\partial x} + \frac{\partial \overline{uv}D}{\partial y} - f\overline{v}D - D\overline{F}_u - G_x - \frac{\tau_{sx} - \tau_{bx}}{\rho_o} = -gD\frac{\partial \eta}{\partial x} - \frac{D}{\rho_o}\frac{\partial p_a}{\partial x} - \frac{g}{\rho_o}\int_{-1}^{0}\left\{J\left[\int_{r}^{0}J\left(\frac{\partial \rho}{\partial x} + \frac{\partial \rho}{\partial r'}\frac{\partial r'}{\partial x}\right)dr'\right]\right\}dr'$$

$$-\frac{1}{\rho_o}\int_{-1}^{0}\left(\frac{\partial qJ}{\partial x} + \frac{\partial qA_1}{\partial r}\right)dr' \tag{2}$$

$$\frac{\partial \overline{v}D}{\partial t} + \frac{\partial \overline{uv}D}{\partial x} + \frac{\partial \overline{v}^2 D}{\partial y} - f\overline{u}D - D\overline{F}_v - G_y - \frac{\tau_{sy} - \tau_{by}}{\rho_o} = -gD\frac{\partial \eta}{\partial y} - \frac{D}{\rho_o}\frac{\partial p_a}{\partial y} - \frac{g}{\rho_o}\int_{-1}^{0}\left\{J\left[\int_{r}^{0}J\left(\frac{\partial \rho}{\partial y} + \frac{\partial \rho}{\partial r'}\frac{\partial r'}{\partial y}\right)dr'\right]\right\}dr'$$

$$-\frac{1}{\rho_o}\int_{-1}^{0}\left(\frac{\partial qJ}{\partial y} + \frac{\partial qA_2}{\partial r}\right)dr' \tag{3}$$

$$G_x = \frac{\partial \overline{u}^2 D}{\partial x} + \frac{\partial \overline{uv} D}{\partial y} - D\tilde{F}_x - \left[\frac{\partial \overline{u^2} D}{\partial x} + \frac{\partial \overline{uv} D}{\partial y} - D\overline{F_x} \right] \tag{4}$$

$$G_y = \frac{\partial \overline{uv} D}{\partial x} + \frac{\partial \overline{v}^2 D}{\partial y} - D\tilde{F}_y - \left[\frac{\partial \overline{uv} D}{\partial x} + \frac{\partial \overline{v^2} D}{\partial y} - D\overline{F_y} \right] \tag{5}$$

where u and v are the x and y components of horizontal velocity, η is the free-surface height, D is the total water column depth ($D = H + \eta$, where H is the reference depth), ρ is density, P_a is air pressure, q is nonhydrostatic pressure, f is the Coriolis parameter, g is gravitational acceleration, τ_s and τ_b are the surface and bottom wind stresses, $J = \partial z / \partial r$, r is the vertical coordinate, $A_1 = J\partial r / \partial x$, $A_2 = J\partial r / \partial y$, F is horizontal momentum diffusion term, and the overbar signifies vertical integration.

To our knowledge, FVCOM has not been used for meteotsunami wave simulation, but has been shown to be well suited for simulating long waves in lakes and coastal systems, similar to the observed conditions during this event [*Anderson and Schwab*, 2013; *Nguyen et al.*, 2014; *Niu et al.*, 2015]. Furthermore, hydrodynamic models with similar construction have shown the ability to resolve the long waves associated with meteotsunami events [*Bechle and Wu*, 2014]. In particular, for wave conditions near coastal boundaries, FVCOM includes a ghost cell boundary approach that deters unrealistic damping of incoming waves and loss of energy in wave reflection. In addition, FVCOM has been successfully applied to a variety of coastal ocean, estuary, and lake environments, including validation of wind-induced surface gravity waves [*Chen et al.*, 2007], tsunami wave generation [*Chen et al.*, 2014], and several barotropic cases [*Huang et al.*, 2008]. In the Great Lakes, FVCOM has been successful in accurately predicting the amplitudes of coastal water level oscillations [*Anderson et al.*, 2010; *Anderson and Schwab*, 2011, 2013; *Niu et al.*, 2015] and other hydrodynamic conditions [*Bai et al.*, 2013; *Fujisaki et al.*, 2013; *Nguyen et al.*, 2014].

The model domain encompasses the entire lake, with a horizontal resolution of 100 m in the central basin (Figure 1, inset). For this event, surface forcing is applied based on spatially and temporally distributed wind stress and pressure, as described above. Model simulation starts at 12:00 GMT on 26 May 2012, with initial conditions supplied by the real-time GLCFS Lake Erie nowcast/forecast model. In order to resolve the fast-moving convective outflows and consequent hydrodynamic response, model results are output on a 30 s time step. The resulting modeled water level displacements at the shoreline are compared to observations from the NOAA/NOS/CO-OPS water level gauges along the southern shore of Lake Erie.

4. Results

4.1. Atmospheric Conditions
Atmospheric conditions are assessed from three sources near Cleveland, OH, including an inland radar tower (KCLE), shoreline ASOS meteorological station (BKL), and offshore buoy (NDBC 45164; Figure 1). Radar radial velocity data (KCLE) reveals that two mesoscale convective systems that pass over the lake yield three distinct outflow bands (two associated with the 17:00 GMT front, and one with the 23 GMT front; Figure 3). Band 1 impacts the Ohio shoreline near 17:30 GMT and contains three outflows (waves) traveling at 14 m/s. Observations from all three nearby sources (radar, shoreline met station, and offshore buoy) record a rapid increase in wind speed from 4 to 12 m/s as a result of the first outflow (Figure 4). Each data source confirms the bandwidth of the waves to be roughly 13 km, yielding a wavelength of 4.5 km and period of 5 min for each outflow. Following this band, the offshore buoy (45164) and shoreline met station (BKL) record sustained winds near 10 m/s. Observations of air pressure reveal the same outflow pattern, with 0.2 mbar/min increases in pressure with the first outflow, followed by 0.15 mbar/min changes in pressure with each subsequent wave. During the same storm front, a second band consisting of a single outflow arrives at the southern shoreline near Cleveland 45 min later and traveling at 19 m/s. Radar detects a 16 m/s radial velocity associated with the outflow, though the shoreline met station (BKL) and offshore buoy (45164) measurements record wind speed just under 15 m/s. Using the radial velocity signature, the wavelength of the outflow is estimated to be 7 km, yielding a period of 6 min. Air pressure recorded at the shoreline met station (BKL) details a single jump in pressure (0.15 mbar/min) associated with Band 2. Band 3, arriving with the second convective front, impacted the Ohio shoreline just before 23:30 GMT. Radar observations show
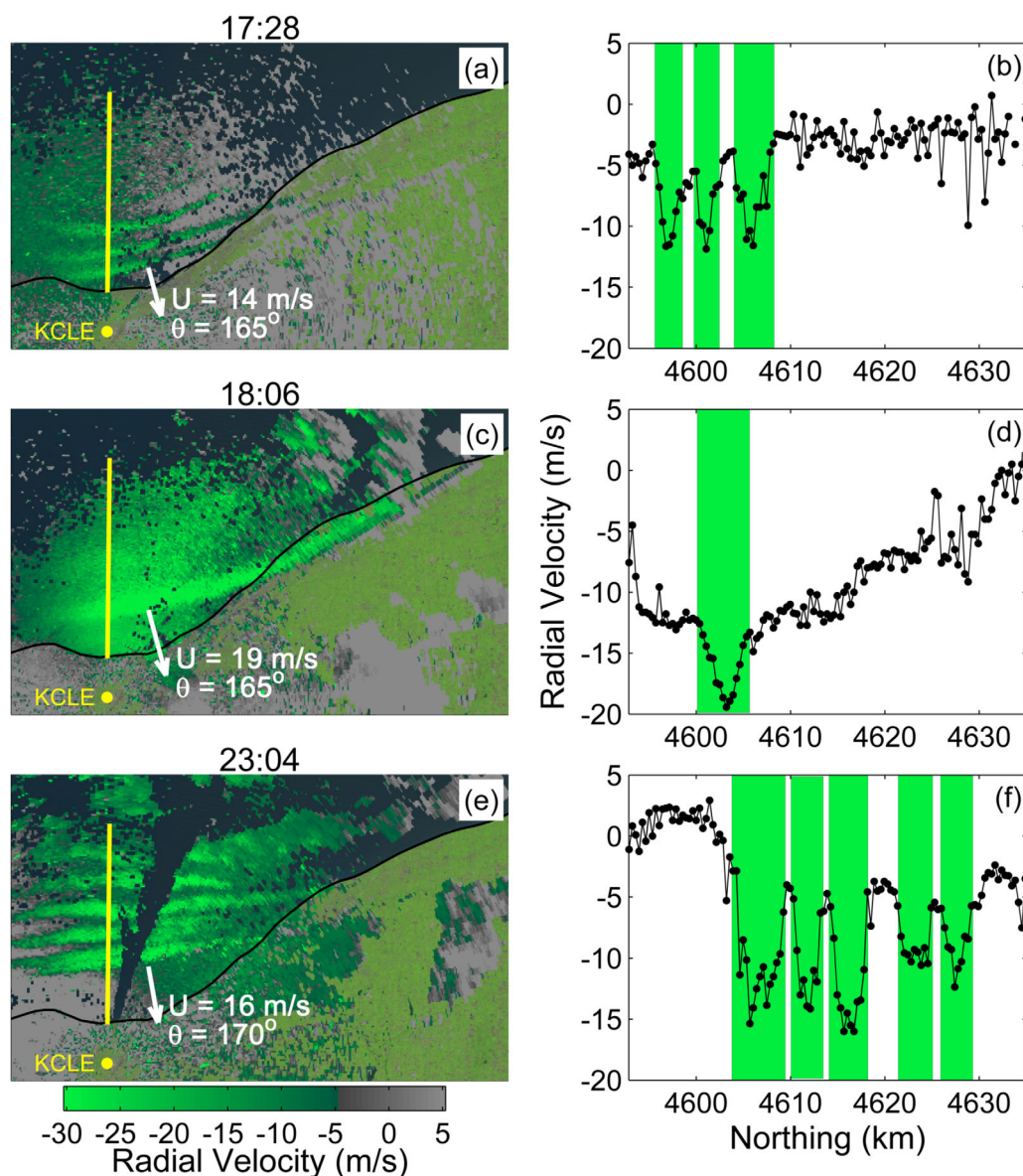
Figure 3. Radial velocity observations on 27 May 2012 illustrate three distinct bands of waves (outflows) as a result of the storm fronts. (top) Band 1 moving at 14 m/s contains three waves with a period of 5 min and wavelength near 4.5 km. (middle) Band 2 contains one outflow wave traveling at 19 m/s, period 6 min, and wavelength of 7 km. (bottom) Band 3 contains five outflow waves, traveling at 17 m/s, with periods of 5 min and wavelength of 5 km. Outflows from each band are highlighted on the right figures.

a series of five outflows associated with the storm front, traveling at a propagation speed of 16 m/s. Observations from the shoreline met station at Cleveland (BKL) show a rise in wind speed from 2 to 14 m/s in under 2 min; however, offshore measurements at the NDBC buoy (45164) reveal wind speeds between 7 and 12 m/s. Using the radial velocity signature, the bandwidth of the outflows is estimated to be 25 km, yielding a wavelength of 5 km and period of 5 min for each wave. Similar to the first convective system, an increase in air pressure occurs with the first outflow (0.6 mbar jump) followed by 0.15 mbar/min changes with each trailing outflow.

For a propagation direction of 165° and average depth, d, of 20 m, the estimated long wave speed in this region of the lake, given by $c = \sqrt{gd}$, where g is acceleration due to gravity, is 14 m/s. Hence, the propagation speed of the outflows is near the long wave speed, $U_{storm} \approx c$, yielding conditions that may have been sufficient to induce Proudman resonance, where energy from the atmospheric disturbance feeds wave amplification in the lake [*Proudman*, 1929].
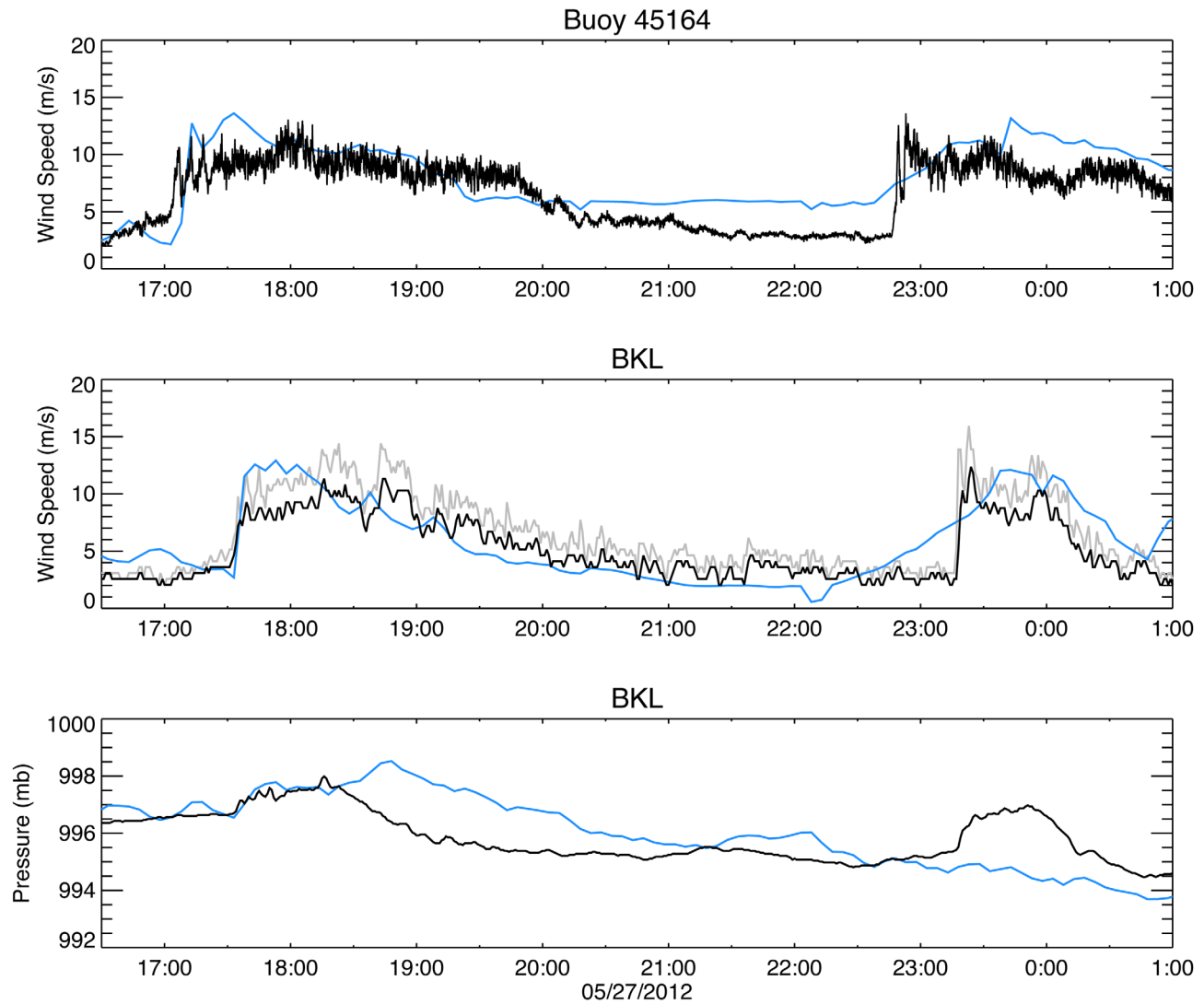
Figure 4. Observed wind speeds and barometric pressure (top) at the NDBC 45164 buoy offshore of Cleveland, OH (1 min data) and (middle and bottom) at the Burke Lakefront Airport (BKL; 2 min average). Observed station data shown in black, wind-gust shown in gray for the BKL station. Simulated 1 km WRF meteorological conditions (case ii) are shown in blue.

4.2. Water Level Fluctuations

Water level observations (6 min) from the NOAA/NOS/CO-OPS stations along the southern shore of Lake Erie depict the arrival of the first water level fluctuations at the Fairport gauge near 17:18 GMT, followed by the Cleveland and Erie gauges to the east and west, respectively (Figure 5). Water level fluctuation amplitudes associated with the first band of outflows are on the order of 10 cm, followed by oscillations at nearly 1 h periods. As the long wave generated from the first atmospheric disturbance would have reflected off the southern shore and back toward the northern coast, which would take 3.17 h based on the shallow water equation, these hourly oscillations in the observed water level at Fairport are likely the result of edge waves. As described in *Ursell* [1952], edge wave speed is governed by

$$c_{edge} = \frac{gT\tan\left[\beta(2n+1)\right]}{2\pi} \tag{6}$$

where g is the acceleration due to gravity, T is the wave period, β is the bottom slope of the beach, and n is the edge wave mode. Therefore, given an estimated slope of 0.0025, computed at the 20 m contour, and a wave period of 60 min, the calculated edge wave speed for the fundamental mode ($n = 0$) is 14.05 m/s. Based on observations from the Fairport and Cleveland gauges, these edge waves appear to travel westward along the southern shore, reaching the Cleveland gauge 45 min after passing the Fairport gauge
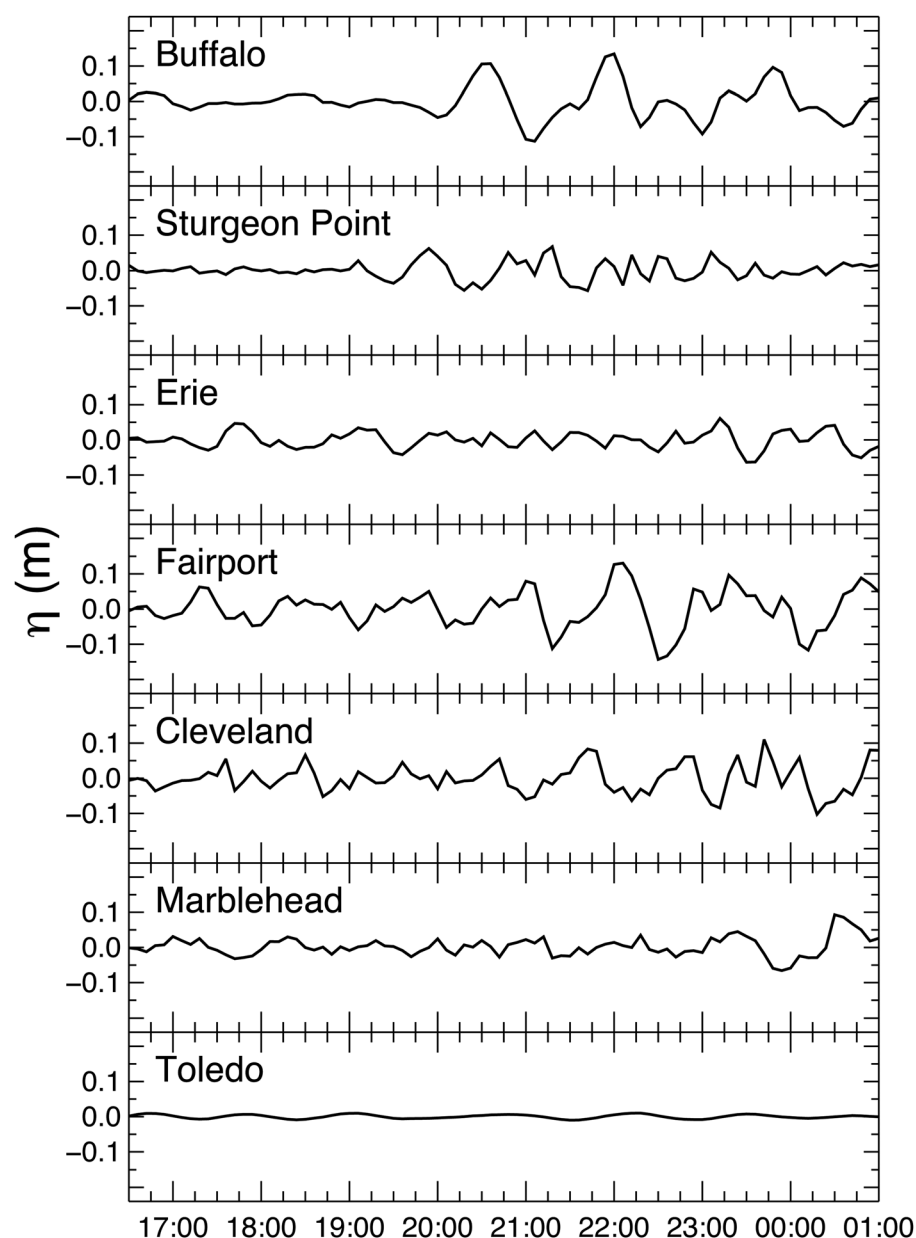
Figure 5. Observed water level displacements (η in m; 6 min records) at the NOS/CO-OPS stations along the southern shore of Lake Erie on 27–28 May 2012 (times in GMT). Water level records are band-pass filtered for oscillations in the meteotsunami spectrum (12 min to 2 h).

(Figure 5). Given that the distance from Fairport Harbor to Cleveland is approximately 40 km, a 45 min travel time confirms the 14 m/s edge wave speed. Further away from the impact location, water level fluctuations at the eastern end of the lake (Buffalo) begin after 20:00 GMT, while the western end of the lake (Toledo) experiences almost no oscillations in the meteotsunami spectrum. With the arrival of the second convective system near 23:00, water level displacements are comparable to those after the impact of the first system. However, observations reveal a set of higher-frequency oscillations occur during this arrival with a period between 10 and 20 min, though the 6 min temporal resolution of the water level gauges makes exact determination difficult.

The largest recorded displacement along the southern shore occurs at the Fairport gauge, when a wave with amplitude of 29 cm is observed near 22:00 GMT, notably larger than the 17:30 displacement that was generated with the first convective system. Its occurrence falls directly between the timing of the two convective systems, yet coincides with the reported time when swimmers were swept into the lake near
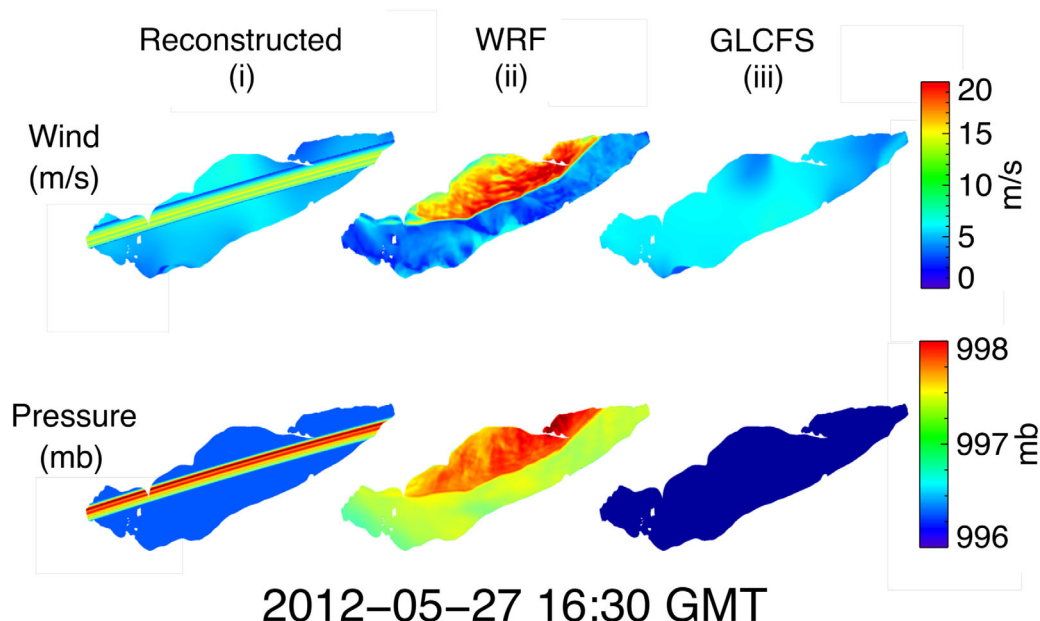
Figure 6. Prescribed atmospheric forcing conditions (wind speed and barometric pressure) for three cases: (i) reconstructed meteorology, (ii) WRF meteorology (1 km), and (iii) GLCFS meteorology at 16:30 GMT on 27 May 2012. The snapshots depict the arrival of the first band of the convective system.

Madison, OH (just west of Fairport). Given the wave train traveling along the edge, as noted above, the 22:00 GMT wave is likely a result of traveling edge waves, possibly with additional energy from wave reflection and focusing from the initial 17:30 convective system. Following this displacement, observations show water level oscillations in the meteotsunami spectrum (12 min to 2 h) continue for the next several hours across the southern shore with displacements between 0.10 and 0.20 m (Figure 5). Overall, the temporal disassociation with the arrivals of the storm bands and the increased amplification raises the questions of what are the specific mechanisms behind the formation of this wave and to what extent is its occurrence a result of the effects of enclosed basins.

4.3. Hydrodynamic Response to Reconstructed and Modeled Meteorology

Using the reconstructed meteorology (case i), model simulation of the convective systems on 27 May 2012 yields a series of waves that coincide with the prescribed meteorology (Figures 6 and 7). The initial storm front (Bands 1 and 2) produce four meteotsunami waves (5 min period) that approach the southern shore, followed by a large trough that trails the wave packet. The waves impact the shoreline (near Fairport water level gauge) just after 17:15 GMT, producing a 0.12–0.16 m rise in water level followed by a 0.30 m drop in 23 min (Figure 8). Water level observations from the Fairport gauge validate the modeled rise in level that coincides with the wave arrival, with the wave crest arriving at 17:18 GMT, 1 min before the largest modeled wave crest; however, the coarse temporal resolution and signal damping at the gauge (6 min) are unable to confirm the individual waves ($T = 5$ min). The observed peak displacement is 0.08 m, which is 50% of the modeled peak displacement of 0.16 m. Furthermore, the observed water level at Fairport does not reveal the dramatic drop in water level near 17:35 GMT predicted by the model, which may be an artifact of the atmospheric reconstruction. Just after 17:30, the model predicts a similar rise in water level at the Cleveland gauge (40 km west of Fairport), which is confirmed by the observed displacement.

Following the initial front (Bands 1 and 2), the reconstructed meteorology simulations yield high-frequency oscillations in water level that persist for the next 3 h. Reflected waves from the first two bands travel to the northern shore of the lake and are reflected again toward to the southern shore (Figure 7; supporting information Animation S1). The concavity of the northern shore in the central basin of Lake Erie sends reflected waves toward the southern shore that coincide in the region east of the Fairport gauge. As the reflected wave impacts the southern shoreline near 21:00 GMT, modeled and observed water level displacements increase in amplitude. The model simulation reveals edge waves along the southern shore that travel
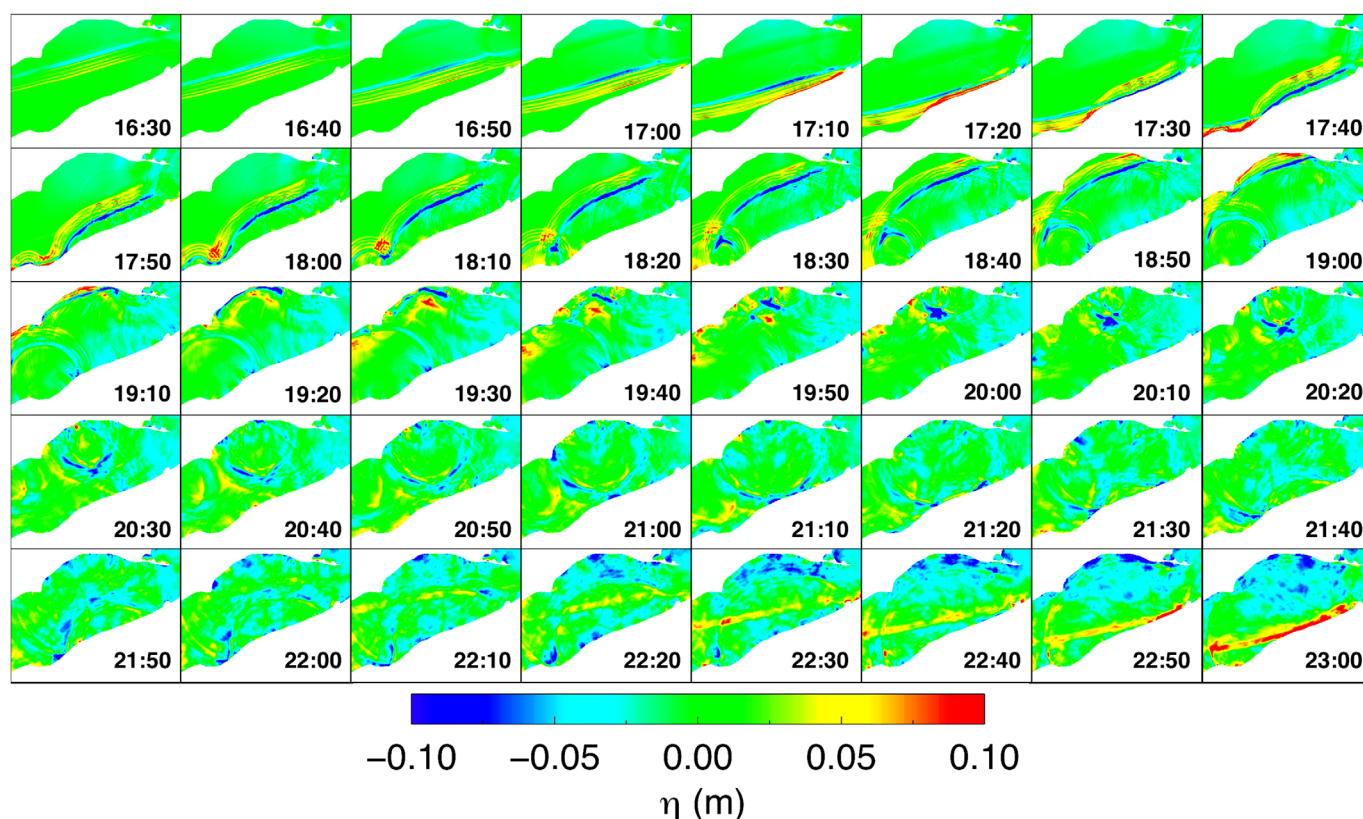
Figure 7. Simulated water level response using the reconstructed meteorology (case i) over Lake Erie on 27 May 2012 (times in GMT). Displacements (η) are shown for the range -0.10 to 0.10 m to highlight wave reflection and refraction, where displacements outside of this range given a constant color (purple or red, respectively).

westward between 21:00 and 22:00 GMT. During the largest observed displacement in water level at 22:00 GMT at Fairport (0.12 m), the reconstructed simulation shows the wave arrival time at 21:53, 7 min before the observed rise, and with a damped peak displacement of 0.09 m. Model simulations show an immediate drop in water level by 0.16 m in 18 min; however, observations reveal a larger displacement of 0.29 m in 30 min.

With the arrival of Band 3 on the southern shore, the simulation using the reconstructed meteorology yields a single wave ($\lambda \approx 5$ km) that impacts Fairport just after 23:00 GMT (23:20 GMT at Cleveland; Figures 7 and 8). The large increase in wind speed and pressure associated with this band causes the largest modeled displacement in the reconstructed simulation (i), where a water level rise of 0.30 m occurs in less than 10 min. However, observed water levels at Fairport and Cleveland show only a 0.11 m rise associated with the third band. Overall, the reconstructed meteorology (case i) yields a root-mean-square deviation (RMSD) of 0.07 and 0.06 m as compared to the gauges at Fairport and Cleveland, respectively, during the meteotsunami event.

In the second hydrodynamic scenario (case ii), a 1 km WRF model is used to drive the water level displacements during the 27 May event (Figure 6). Though a similar front is modeled for wind and pressure as compared to the idealized reconstructed meteorology (case i), the WRF simulation depicts a much more spatially complex overwater meteorological field (Figure 9; supporting information Animation S2). Additionally, the timing of the systems (Bands 1–3) is well represented by the WRF simulation as compared to observations (Figure 4). Hydrodynamic response to the WRF modeled meteorology (ii) reveals a large wave and water level displacement along the southern shoreline as a result of the first two bands (Figures 8 and 10). The initial rise in water level at Fairport and Cleveland comes 16 min later than the observed water level displacement. Amplitudes of the response are 0.20 m at Fairport and 0.19 m at Cleveland. At both locations, the water level rise is followed by a drop in level over 0.30 m, though less pronounced than in the reconstructed meteorology case. Following the arrival of this wave at the southern shore, the model results show
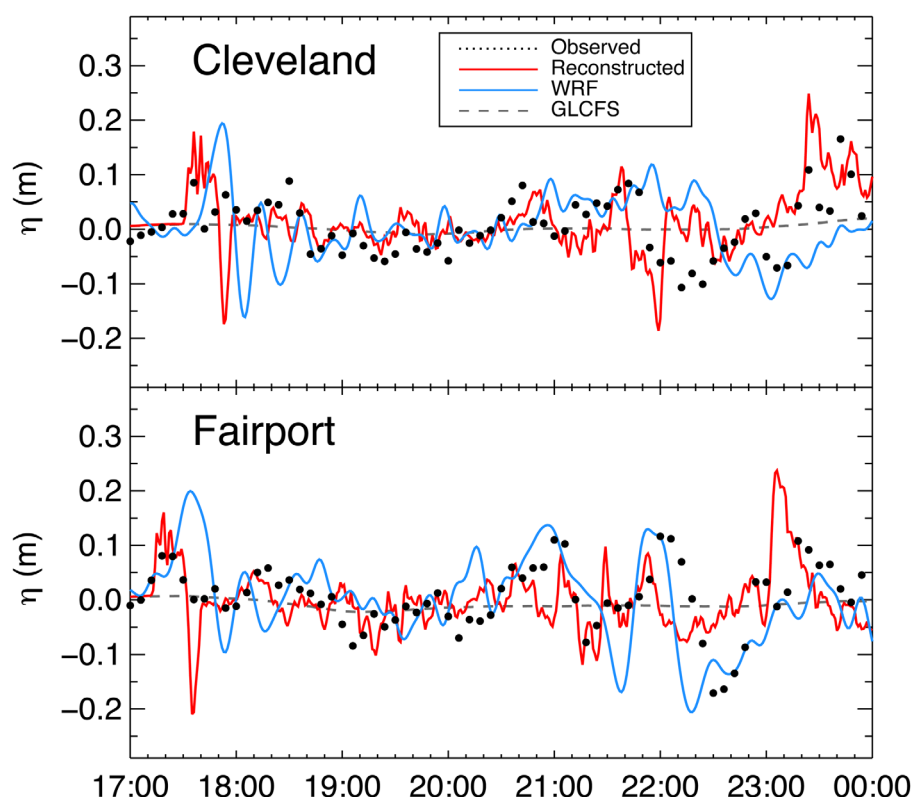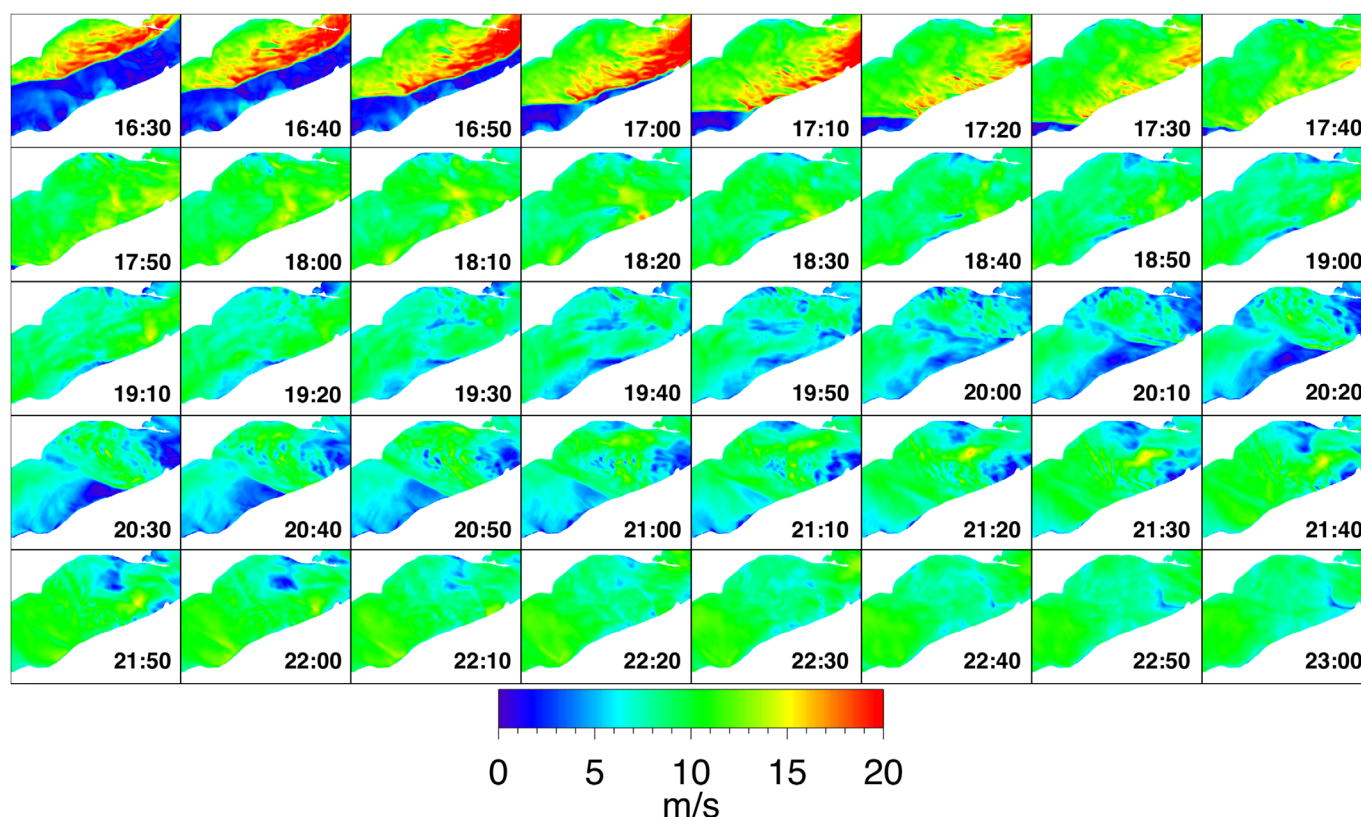
Figure 8. Water level displacements (η; 1 min) at the Cleveland (NOS/CO-OPS 9063063) and Fairport (NOS/CO-OPS 9063053) gauge locations on 27 May 2012 (time in GMT). Model water level displacements are shown for the (i) reconstructed meteorology, (ii) WRF meteorology (1 km), and the (iii) GLCFS meteorology cases. Observed water level displacements are shown at each gauge (black circles; 6 min).

a similar wave reflection toward the northern shore as seen in the reconstructed meteorology case, which arrives around 19:00 GMT and is reflected again toward the southern shore of the lake (Figure 10; supporting information Animation S3). However, in this case ii, the model reveals a rise in water level (0.14 m) at the Fairport gauge at 21:56 GMT, just 4 min before the observed water level shows a similar rise (0.11 m). The FVCOM simulation shows a series of edge waves that move westward along the southern shore between 20:30 and 22:30 GMT.

At 22:00 GMT, near the time when three swimmers were reportedly swept a 0.5 mi into the lake, the modeled wave arrives 7 min before the observed displacement, similar to the previous case; however, the model wave height (0.13 m) is closer to the observed peak displacement (0.12 m) at the Fairport gauge (Figure 8). Similarly, the WRF-driven simulation predicts the large water level drawdown that immediately follows an overall drop of 0.34 m in 25 min. The modeled low water level comes 10 min before the observed trough, though the magnitude of the simulated displacement (−0.21 m) closely matches the observed level (−0.17 m). Contour plots of the modeled water level displacement reveal an edge wave that appears between Madison and Fairport between 21:00 and 22:00 GMT and travels west along the shore toward Cleveland (Figure 10; supporting information Animation S3). Overall, the RMSD between this case and the observed water levels is 0.07 m for both the Fairport and Cleveland gauges. Snapshots of the modeled current field near the Madison, OH, illustrate the passage of this edge wave (Figure 11). Initially, a westward longshore flow exists at 21:00 GMT, thereafter, a reversal in longshore flow occurs at 21:15 with increased nearshore current structure and an offshore flow near 21:25. Finally, with the passage of the wave, a strong westward longshore current develops by 21:45 GMT and is sustained for the next few hours.

As a baseline for comparison, in case iii, the hydrodynamic model is simulated using the GLCFS meteorology, which is the current operational method for hydrodynamic forecasting in the Great Lakes (Figure 6). In this scenario, predicted water level displacements are less than 3 cm during the entire event (Figure 8). The largest displacement occurs after 23:00 GMT with the arrival of the second convective system (Band 3), though because the station-based interpolation method does not resolve the fine-scale nature of the storm

Figure 9. Simulated wind speed in the 1 km WRF meteorology case, as depicted over Lake Erie on 27 May 2012 (times in GMT).

conditions, even these small displacements are not in phase with the observed water level displacements. Although interpolation of the meteorology from land-based stations generally yields good agreement with observed water levels throughout the year [*Schwab and Bedford*, 1994], investigation of meteotsunami-scale frequencies reveals the inadequacy of the current operational approach to resolve any of the features of the 27 May event.

5. Discussion

5.1. Radial Velocity for Meteotsunami Storm Detection

This study demonstrates the utility of mean radial velocity radar data in the detection of meteotsunami-causing atmospheric disturbances which to date has yet to be used in this application. Mean radial velocity depicts the movement of scattering particles moving toward and away from a Doppler radar, yielding the combined velocity of the storm movement and wind speed in the direction parallel to the radar beam [*Crum and Alberty*, 1993; *Klazura and Imy*, 1993]. Mean radial velocity is useful in the detection and measurement of intense wind phenomena such as mesocyclones [*Stumpf et al.*, 1998], gust fronts [*Klingle et al.*, 1987], and downbursts [*Roberts and Wilson*, 1989]. For the 27 May, meteotsunami event, mean radial velocity imagery from KCLE (Figure 3) provided a spatial measurement of the meteotsunami-causing outflows. The propagation speed and direction of the outflows was determined from the displacement of the high-velocity regions throughout a time series of scans, indicating that Band 1 was moving toward the shore at the Proudman resonant speed of Lake Erie. The outflows moved nearly parallel to the direction of the north-oriented radar beam so the raw radial velocities provided a reasonable approximation of the outflow wind speed magnitude. Indeed, the radial velocity cross sections along this beam (Figures 3b, 3d, and 3f) match the observed wind speeds at the BKL station (Figure 4) within 2 m/s for Bands 1 and 3 and within 5 m/s for Band 2. Furthermore, the radial velocity data depict the spatial scale of the outflows in each band, consistent with the fluctuations and gradients in the atmospheric pressure data. The mean radial velocity data were the key meteorological observation which facilitated the reconstruction of the 27 May Lake Erie
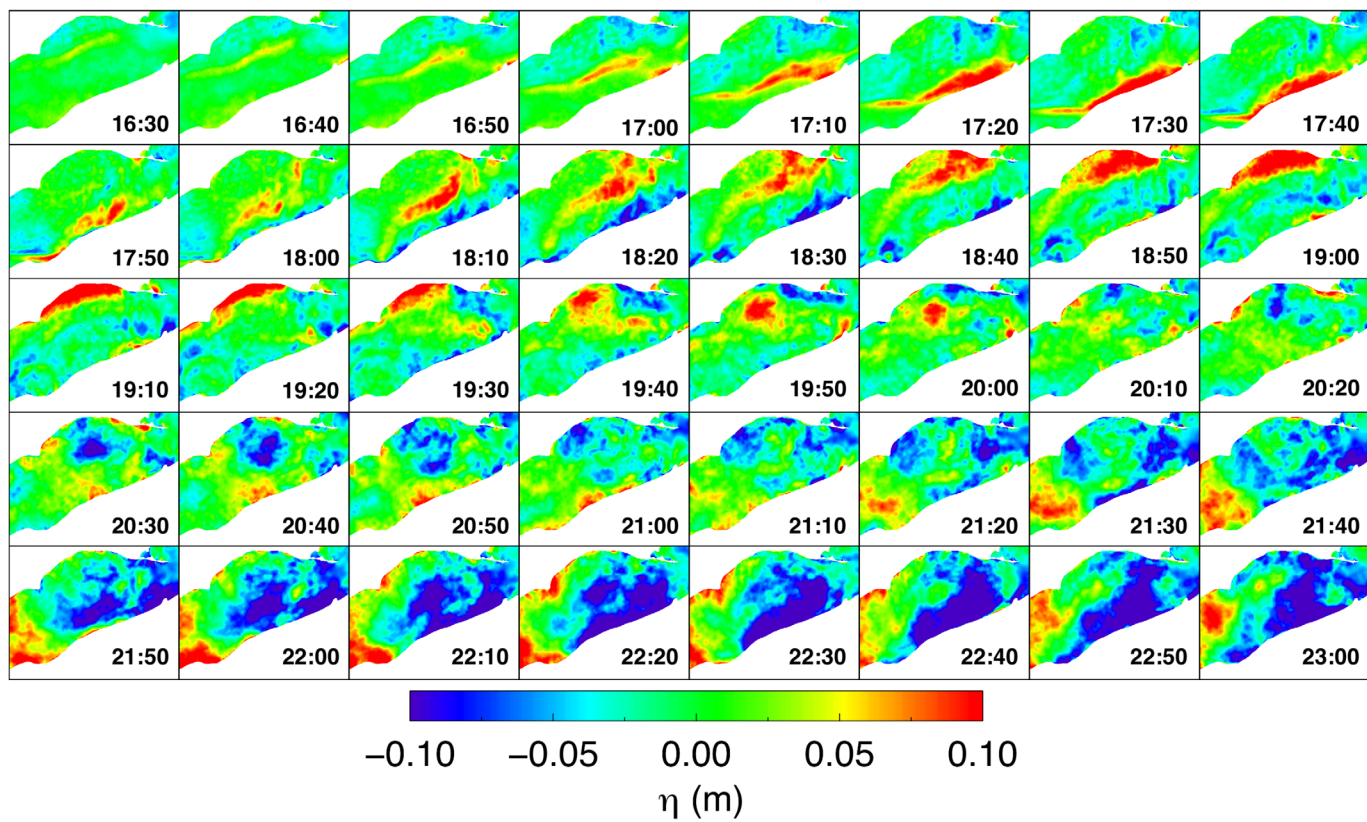
Figure 10. Simulated water level response using WRF meteorology (case ii) over Lake Erie on 27 May 2012 (times in GMT). Displacements (η) are shown for the range -0.10 to 0.10 m to highlight wave reflection and refraction, where displacements outside of this range given a constant color (purple or red, respectively).

meteotsunami event, providing not only the propagation speed and direction of the outflows but also the magnitude and spatial structure of the wind surface forcing.

The value of the radial velocity data is apparent when considering the 27 May meteotsunami-causing atmospheric disturbances passed through the network of meteorological observations along the shore of Lake Erie unnoticed in real time. Though strong pressure fluctuations and increases in wind speed were observed at the BKL, HZY, and ERI ASOS stations as the meteotsunami-producing disturbance crossed the southern shoreline of Lake Erie near Cleveland (17:30), this surface data alone could not characterize the atmospheric disturbance movement due to limitations in gauge orientation. To calculate the speed and direction of the atmospheric disturbance, meteotsunami detection protocols in place in the Adriatic [*Šepić et al.*, 2009; *Šepić and Vilibić*, 2011] and the Mediterranean [*Andre et al.*, 2013] utilize the arrival times of atmospheric pressure fluctuations at multiple spatially distributed gauges [*Orlić*, 1980]. Nevertheless, the ASOS meteorological stations near Lake Erie are distributed in a one-dimensional linear manner following the lake shore (Figure 1), which greatly limits the ability to calculate the horizontal motion of the disturbance. While overwater observations are available from buoys such as NCDC 45164, these stations only report wind speeds and pressure at 10 min intervals in real time and are limited to only a few locations in each of the Great Lakes. The meteotsunami-causing outflow bands were also difficult to discern in radar reflectivity data. While radar reflectivity imagery has been used to provide spatial depiction of other meteotsunami-producing atmospheric disturbances [*Churchill et al.*, 1995; *Pellikka et al.*, 2014; *Wertman et al.*, 2013] , in these cases the pressure and wind disturbances were associated with strong reflectivity signals of convective storms. In the 27 May meteotsunami, the intense radar reflectivity cells of the convective storms never passed over the Cleveland area (Figure 2) even though strong pressure and wind perturbations were observed at BKL. Only in the radial velocity imagery are the meteotsunami-causing outflows apparent over the lake.

This study also demonstrates the potential for mean radial velocity radar data to be used as a tool for real-time meteotsunami prediction, supplementing gaps in overwater observations that exist in surface
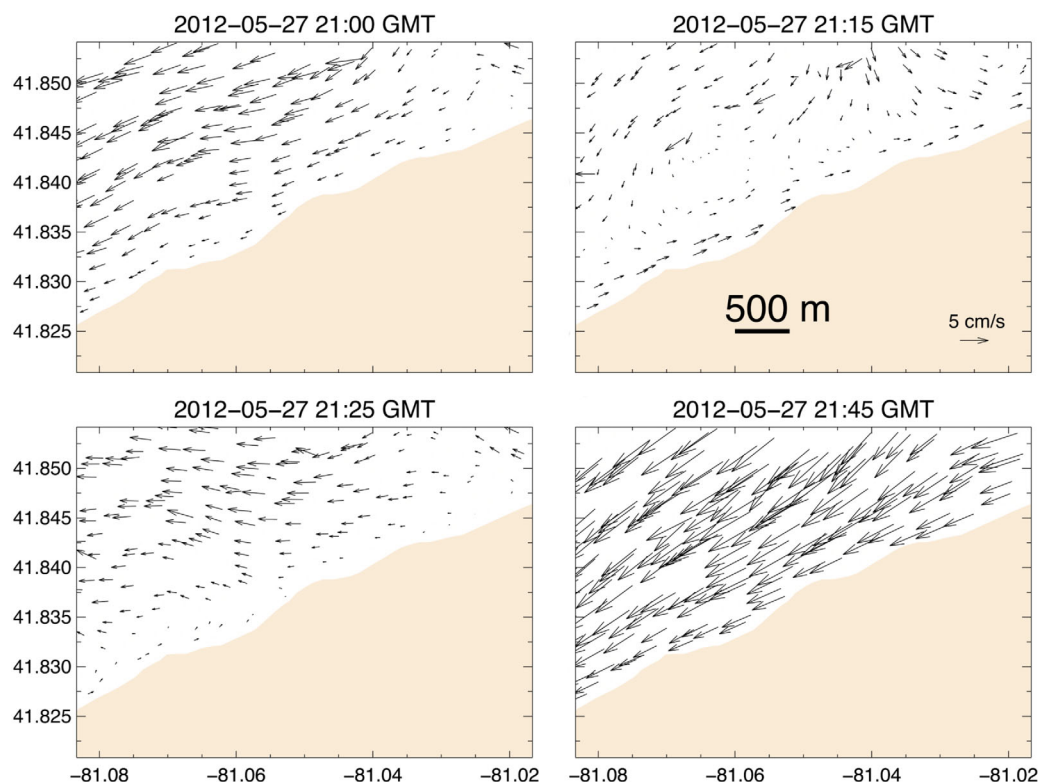
Figure 11. FVCOM simulated vertically averaged currents near Madison, OH, using the 1 km WRF meteorology (case ii). Currents depict beach-scale conditions during the arrival of the large water level displacement near 22:00 GMT.

meteorology networks. For example, the Band 1 outflows were observable in the mean radial velocity data moving over the lake at the Proudman resonant speed (14 m/s) beginning at 17:00, 30 min prior to the arrival of the initial meteotsunami wave at the Cleveland area at 17:30. These observations of the Proudman resonant disturbance could have provided valuable warning of a potential meteotsunami to forecasters. Thus, the WSR-88D Doppler radar network could serve as a vital data source for meteotsunami early warning, as the radar network covers nearly all of the U.S. Great Lakes and Atlantic coastlines [*Maddox et al.*, 2002]. Similar detection could be facilitated through Doppler radars along other meteotsunami-prone coasts, such as those in the Operational Program for Exchange of Weather Radar Information (OPERA) network in Europe [*Huuskonen et al.*, 2014]. Overall, mean radial velocity observations have great potential to improve both the characterization of meteotsunami-causing atmospheric disturbances as well as the prediction of meteotsunami events.

5.2. Sensitivity to Wind and Pressure Perturbations
To understand the role of the pressure and the wind stress components of the atmospheric disturbance in the formation of the meteotsunami wave, the respective terms in the shallow water equations are computed and compared following the procedures of *Churchill et al.* [1995] and *Orlić et al.* [2010]. The atmospheric pressure term of the shallow water equations is given by $\partial(P/\rho)/\partial x$, where P is the atmospheric pressure and ρ is the density of water. The wind term of the shallow water equations is $\tau/\rho H$, where ρ is the density of water, H is water depth, and τ is the wind stress with drag coefficient calculated from the formulation of *Large and Pond* [1981]. The averaged atmospheric pressure and wind terms are calculated from the reconstructed meteorology time series for each of the three storm bands that cross the lake. The first band (17:30–17:50) is dominated by pressure perturbations, with an average pressure term of 1.5×10^{-5} m/s^2 and wind stress term of 7.6×10^{-6} m/s^2, yielding a partition of 66% pressure to 34% wind stress. The second band (18:10–18:20) has an average pressure term of 5.1×10^{-6} m/s^2 and average wind stress term of 6.8×10^{-6} m/s^6 (43% pressure to 57% wind). The third band (23:15–23:45) has and average pressure term of 1.3×10^{-5} m/s^2 and average wind stress term of 1.8×10^{-5} m/s^2 (41% pressure to 59% wind). Similar partitioning of atmospheric pressure and wind stress influence on water level fluctuations are obtained

when comparing hydrodynamic model runs forced with only the atmospheric pressure component of the reconstructed meteorology and only the wind stress component of the reconstructed meteorology.

As the waves that struck the Cleveland area at 17:30 and 22:00 are attributed to the first band of surface forcings (Figures 7 and 10; supporting information Animation S1 and S3), this analytical analysis suggests that the dominant forcing of these destructive waves was atmospheric pressure fluctuations, though wind stress accounts for a third of the wave height. While wind speeds never exceeded 13 m/s in Band 1, the wind stress term is relatively large in shallow Lake Erie. Conversely, similar wind speeds (10–15 m/s) are deemed negligible in meteotsunami generation in the deeper Adriatic and Mediterranean Seas [*Orlić et al.*, 2010; *Renault et al.*, 2011; *Šepić et al.*, 2015]. Even in regions where wind stress has been noted to be a significant driver of meteotsunamis such as the Gulf of Finland [*Pellikka et al.*, 2014], the Western Australia coast [*Pattiaratchi and Wijeratne*, 2014], and Lake Michigan [*Platzman*, 1965; *Bechle and Wu*, 2014], wind speeds associated with meteotsunamis typically exceed 25 m/s. For example, when the Band 1 disturbance is applied to depths characteristic of Lake Michigan (∼80 m), the wind stress term is minor (<10% partition) relative to atmospheric pressure. Thus, the shallow depths of Lake Erie make meteotsunamis in this basin highly sensitive to wind stress events.

5.3. Atmospheric Modeling

Significant challenges exist in simulating and replicating salient features of transient mesoscale convection systems. This is especially true under weakly forced synoptic-scale conditions, as presented during the period of interest. To optimize the atmospheric forcing for this event, a series of WRF sensitivity tests are performed varying initial starting time, implicit physics parameterizations (e.g., boundary layer, microphysics—including double moment schemes), surface boundary conditions (e.g., lake surface temperature data sources), and initial and boundary conditions (in this case NARR and NCEP Rapid Update Cycle - RUC analyses).

The greatest contributor to a successful simulation of the convective systems' evolution is establishing an initial start time before the diurnal convection cycle of the day prior (12 GMT, 26 May). This allows the simulation to completely encapsulate the entire development and maturation of the initial long-lived convective system. For completeness, the optimized WRF setup is determined to be a combination of NARR initial and boundary conditions, Goddard single moment microphysics [*Tao et al.*, 1989], and ACM2 boundary layer [*Pleim*, 2007] with use of the RTG 1/12th degree [*Gemmill et al.*, 2007] lake surface temperatures. The result is a simulation of two distinct convective systems separated by a similar amount of time as compared to observations, and at the appropriate amplitude and spatial footprint, which exceeds expectations given the weakly constrained atmospheric conditions for the mesoscale convective systems to develop and operate. Although additional testing with alternate boundary conditions and microphysics may lead to improved simulations in certain respects, the scope of this work is to provide a reasonable estimation of the atmospheric forcing conditions during the 27 May 2012 event in an effort to detail the processes associated with meteotsunami conditions in the Great Lakes.

5.4. Effects of an Enclosed Basin on Hydrodynamic Response

The wave transformation processes that occurred in this event illustrate the unique threat posed by of meteotsunamis in enclosed basins. Wave heights in excess of the initial meteotsunami wave, which struck the Cleveland area at 17:30, were achieved through wave reflection, spatial focusing, and edge wave generation. Model simulations reveal that the formation of the destructive meteotsunami wave near Madison, OH, at 22:00 was the product of a wave initially generated by the first band of atmospheric disturbances, which struck the Cleveland area around 17:30 and reflected northward off of the coast. When this wave subsequently reflected off the concave northern coast, the reflected wave was spatially focused as it propagated southward back toward the southern shore, meeting in the vicinity east of Fairport Harbor, OH, with a greater height than the initial wave at 17:30. The combination of these waves produced edge waves that traveled westward along the shoreline, resulting in a dramatic water level rise and subsequent drawdown at a time when wind speeds were low and atmospheric conditions were relatively calm. Model simulations reveal the formation of these waves near Madison, OH, through reflection and focusing processes and give us insight into the mechanisms behind the development of meteotsunami waves in enclosed basins.

This event demonstrates that meteotsunami reflection in enclosed basins can separate the waves from the causative meteorology. In this case, the largest modeled and observed water level displacements occurred at 22:00, nearly 4.5 h after the initial meteorological disturbance (Band 1) crossed the shoreline (17:30) and 1 h before the another system reached the coast (Band 3 at 23:00). Indeed, two of the three reported destructive and life-threatening incidents occurred in the time between these storms in a period of relatively calm meteorological conditions. In this manner, the disassociation between the causal forces and the meteotsunami wave conditions resembles the threat associated with many seismic tsunamis though owing to the slower propagation speed of meteotsunamis, this time lag is on the order of a few hours. Over the course of this time span, the public perception may be that the threat associated with a convective storm is over, causing a return to normal recreational and commercial use of the lake, increasing the danger posed by the meteotsunami wave. The disassociation of a meteotsunami wave from the causative meteorology due to reflection was noted to be a factor in the fatal 1954 Lake Michigan meteotsunami [*Ewing et al.*, 1954]. The effects of wave reflection are not limited only to enclosed basins, as a steep continental shelf break acts as a boundary to reflect offshore-propagating meteotsunami waves back to the U.S. East Coast [*Pasquet and Vilibić*, 2013; *Lipa et al.*, 2014].

6. Conclusions

Many questions still remain in regard to meteotsunami formation and the threat posed by impacts on coastal communities although extensive research has been carried out to understand and document meteotsunami events around the world [*Jansa et al.*, 2007; *Candella*, 2009; *Dragani et al.*, 2009; *Šepić et al.*, 2009; *Thomson et al.*, 2009; *Asano et al.*, 2012; *Pasquet and Vilibić*, 2013; *Vilibić et al.*, 2014]. Recent work has also described the danger associated with reflected waves [*Pasquet and Vilibić*, 2013; *Lipa et al.*, 2014] and the unique threats posed by edge waves and wave focusing due to enclosed basins such as the Great Lakes [*Bechle and Wu*, 2014; *Šepić and Rabinovich*, 2014]. In this work, we build on this understanding by investigating the 27 May 2012 meteotsunami event in Lake Erie, which impacted swimmers, recreational boaters, and marinas along the U.S. shoreline. Through analysis of the radial velocities from a nearby radar tower and other coastal meteorological observations, a reconstructed meteorological field is used in conjunction with modeled atmospheric forcing conditions to drive a high-resolution hydrodynamic model of Lake Erie. Although difficulties still remain in simulating convective systems that induce meteotsunamis and the meteotsunami waves themselves, the atmospheric and hydrodynamic approaches used in this study allow for the elucidation of the underlying processes behind meteotsunami creation. It is determined that the first of two convective systems traveling from the north across the lake generated a series of waves in the meteotsunami band that reflected off of the southern and then northern shores of the lake, which upon the return to the southern shore produced edge waves that traveled along the coast that swept three swimmers 0.5 mi into the lake and inundated a marina several minutes later. These processes detail the effects of enclosed basins with regard to wave reflection and focusing of wave energy, and in particular the temporal differences between the passing of the convective storm and the arrival of the meteotsunami waves. Furthermore, as found in a hindcast investigation of the Chicago 1954 meteotsunami event [*Bechle and Wu*, 2014], both pressure changes and rapid increases in wind speed play an important role in the meteotsunami development in Lake Erie. Although several historical cases have been reclassified as potential meteotsunami cases, this work presents a recent case of meteotsunami detection and impact to the coastal community and describes the processes that led to meteotsunami formation in Lake Erie.

Overall, the difficulty in documenting these conditions in this study may not be a function of rarity, but rather a result of the present infrastructure used to observe and model meteotsunamis in the Great Lakes. Due to the fine-scale spatial extent of these convective systems, their sharp gradients in wind stress and air pressure, and the propagation speed of these storms, the atmospheric conditions that produce meteotsunami waves in the Great Lakes often pass undetected through observational networks. In addition, limitations in atmospheric conditions cause difficulties in adequately resolving the resultant meteotsunami outcomes. In fact, these destructive storms inhabit blind spots in the present observational and operational systems. As a result, very few meteotsunami events have been reported in the Great Lakes to date. Thus, the use of remote sensing observations such as radar radial velocity as well as next-generation atmospheric and hydrodynamic modeling systems are crucial to improve our ability to understand the mechanisms that cause meteotsunamis and how their frequency and intensity might change with increasingly frequent

strong convective events [*Bentley and Sparks*, 2003; *Ashley et al.*, 2005]. As enclosed basins, the Great Lakes may pose a unique set of conditions with regard to meteotsunamis, and the ability to detect these extreme storms and predict the hydrodynamic response is crucial to reducing risk and building resilient coastal communities.

References

Anderson, E. J., and D. J. Schwab (2011), Relationships between wind-driven and hydraulic flow in Lake St. Clair and the St. Clair River Delta, *J. Great Lakes Res.*, *37*(1), 147–158.

Anderson, E. J., and D. J. Schwab (2013), Predicting the oscillating bi-directional exchange flow in the Straits of Mackinac, *J. Great Lakes Res.*, *39*(4), 663–671.

Anderson, E. J., D. J. Schwab, and G. A. Lang (2010), Real-time hydraulic and hydrodynamic model of the St. Clair River, Lake St. Clair, Detroit River System, *J. Hydraul. Eng.*, *136*(8), 507–518.

Andre, G., M. Marcos, and C. Daubord (2013), Detection method of meteotsunami events and characterization of harbor oscillations in Western Mediterranean, *Coastal Dynamics 2013 conference proceedings*, 24–28 June 2013, pp. 83–92.

Asano, T., T. Yamashiro, and N. Nishimura (2012), Field observations of meteotsunami locally called ''abiki'' in Urauchi Bay, Kami-Koshiki Island, Japan, *Nat. Hazards*, *64*(2), 1685–1706.

Ashley, W. S., T. L. Mote, and M. L. Bentley (2005), On the episodic nature of derecho-producing convective systems in the United States, *Int. J. Climatol.*, *25*(14), 1915–1932, doi:10.1002/joc.1229.

As-Salek, J., and D. Schwab (2004), High-frequency water level fluctuations in Lake Michigan, *J. Waterw. Port Coastal Ocean Eng.*, *130*(1), 45–53, doi:10.1061/(ASCE)0733-950X(2004)130:1(45).

Bai, X., J. Wang, D. J. Schwab, Y. Yang, L. Luo, G. A. Leshkevich, and S. Liu (2013), Modeling 1993-2008 climatology of seasonal general circulation and thermal structure in the Great Lakes using FVCOM, *Ocean Modell.*, *65*, 40–63.

Bechle, A. J., and C. H. Wu (2014), The Lake Michigan meteotsunamis of 1954 revisited, *Nat. Hazards*, *74*, 155–177, doi:10.1007/s11069-014-1193-5.

Bentley, M. L., and J. A. Sparks (2003), A 15 yr climatology of derecho-producing mesoscale convective systems over the central and eastern United States, *Clim. Res.*, *24*(2), 129–139, doi:10.3354/cr024129.

Candela, J., S. Mazzola, C. Sammari, R. Limeburner, C. J. Lozano, B. Patti, and A. Bonanno (1999), The ''Mad Sea'' phenomenon in Strait of Sicily, *J. Phys. Oceanogr.*, *29*(9), 2210–2231.

Candella, R. N. (2009), Meteorologically induced strong seiches observed at Arraial do Cabo, RJ, Brazil, *Phys. Chem. Earth*, *34*(17–18), 989–997, doi:10.1016/j.pce.2009.06.007.

Chen, C., H. Liu, and R. C. Beardsley (2003), An unstructured grid, finite-volume, three-dimensional, primitive equations ocean model: Application to coastal ocean and estuaries, *J. Atmos. Oceanic Technol.*, *20*(1), 159–186.

Chen, C., R. C. Beardsley, and G. Cowles (2006), An unstructured grid, finite-volume coastal ocean model (FVCOM) system, *Oceanography*, *19*(1), 78–89.

Chen, C., H. Huang, R. C. Beardsle, H. Liu, Q. Xu, and G. Cowles (2007), A finite-volume numerical approach for coastal ocean circulation studies: Comparisons with finite difference models, *J. Geophys. Res.*, *112*, C03018, doi:10.1029/2006JC003485.

Chen, C., Z. Lai, R. C. Beardsley, J. Sasaki, J. Lin, H. Lin, R. Ji, and Y. Sun (2014), The March 11, 2011 Tohoku M9.0 earthquake-induced tsunami and coastal inundation along the Japanese coast: A model assessment, *Prog. Oceanogr.*, *123*, 84–104, doi:10.1016/j.pocean.2014.01.002.

Churchill, D. D., S. H. Houston, and N. A. Bond (1995), The Daytona Beach wave of 3-4 July 1992—A shallow-water gravity-wave forced by a propagating squall line, *Bull. Am. Meteorol. Soc.*, *76*(1), 21–32, doi:10.1175/1520-0477(1995)076 < 0021:TDBWOJ>2.0.CO;2.

Cleveland Plain Dealer (1882), A Tidal Wave Sweeps the Lake Front, Doing Considerable Damage–Docks Four Feet Under Water–Hundreds of Fish Washed Ashore.

Crum, T. D., and R. L. Alberty (1993), The WSR-88D and the WSR-88D operational support facility, *Bull. Am. Meteorol. Soc.*, *74*(9), 1669–1687.

Donn, W. L., and N. K. Balachandran (1969), Coupling between a moving air-pressure disturbance and the sea surface, *Tellus*, *21*(5), 701–706, doi:10.1111/j.2153-3490.1969.tb00478.x.

Dragani, W. C., E. E. D'Onofrio, W. Grismeyer, M. M. E. Fiore, and M. I. Campos (2009), Atmospherically-induced water oscillations detected in the port of Quequén, Buenos Aires, Argentina, *Phys. Chem. Earth*, *34*, 998–1008.

Ewing, M., F. Press, and W. L. Donn (1954), An explanation of the Lake Michigan wave of 26 June 1954, *Science*, *120*(3122), 684–686, doi:10.1126/science.120.3122.684.

Fujisaki, A., J. Wang, X. Bai, G. Leshkevich, and B. Lofgren (2013), Model-simulated interannual variability of Lake Erie ice cover, circulation, and thermal structure in response to atmospheric forcing 2003-2012, *J. Geophys. Res. Oceans*, *118*, 4286–4304, doi:10.1002/jgrc.20312.

Gemmill, W., B. Katz, and X. Li (2007), Daily real-time global sea surface temperature high-resolution analysis: RTG_SST_HR NOAA/NCEP, *NOAA/NWS/NCEP/MMAB Off. Note 260*, 39 pp., NOAA, College Park, Md.

Huang, H., C. Chen, G. W. Cowles, C. D. Winant, R. C. Beardsley, K. S. Hedstrom, and D. B. Haidvogel (2008), FVCOM validation experiments: Comparisons with ROMS for three idealized barotropic test problems, *J. Geophys. Res.*, *113*, C07042, doi:10.1029/2007JC004557.

Huuskonen, A., E. Saltikoff, and I. Holleman (2014), The operational weather radar network in Europe, *Bull. Am. Meteorol. Soc.*, *95*, 897–907.

Jansa, A., S. Monserrat, and D. Gomis (2007), The rissaga of 15 June 2006 in Ciutadella (Menorca), a meteorological tsunami, *Adv. Geosci.*, *12*, 1–4.

Klazura, G. E., and A. A. Imy (1993), A description of the initial set of analysis products available from the NEXRAD WSR-88D system, *Bull. Am. Meteorol. Soc.*, *74*(7), 1293–1311.

Klingle, D. L., D. R. Smith, and M. M. Wolfson (1987), Gust front characteristics as detected by Doppler radar, *Mon. Weather Rev.*, *115*, 905–918, doi:10.1175/1520-0493(1987)115 < 0905:GFCADB>2.0.CO;2.

Large, W. G., and S. Pond (1981), Open ocean momentum flux measurements in moderate to strong winds, *J. Phys. Oceanogr.*, *11*, 324–336, doi:10.1175/1520-0485(1981)011 < 0324:OOMFMI>2.0.CO;2.

Lipa, B., H. Parikh, D. Barrick, H. Roarty, and S. Glenn (2014), High-frequency radar observations of the June 2013 US East Coast meteotsunami, *Nat. Hazards*, *74*(1), 109–122, doi:10.1007/s11069-013-0992-4.

Maddox, R. A., J. Zhang, J. J. Gourley, and K. W. Howard (2002), Weather radar coverage of the contiguous United States, *Weather Forecasting*, *17*, 927–934.

Mesinger, F., et al. (2006), North American regional reanalysis, *Bull. Am. Meteorol. Soc.*, *88*(3), 343–360.

Monserrat, S., I. Vilibić, and A. B. Rabinovich (2006), Meteotsunamis: Atmospherically induced destructive ocean waves in the tsunami frequency band, *Nat. Hazards Earth Syst. Sci.*, *6*(6), 1035–1051, doi:10.5194/nhess-6-1035-2006.

New York Times (1912), Tidal Wave Sweeps Erie.

Nguyen, T. D., P. Thupaki, E. J. Anderson, and M. S. Phanikumar (2014), Summer circulation and exchange in the Saginaw Bay-Lake Huron system, *J. Geophys. Res. Oceans*, *119*, 2713–2734, doi:10.1002/2014JC009828.

Niu, Q., M. Xia, E. S. Rutherford, D. M. Mason, E. J. Anderson, and D. J. Schwab (2015), Investigation of interbasin exchange and interannual variability in Lake Erie using an unstructured-grid hydrodynamic model, *J. Geophys. Res. Oceans*, *120*, 2212–2232, doi:10.1002/2014JC010457.

Orlić, M., D. Belusic, I. Janekovic, and M. Pasaric (2010), Fresh evidence relating the great Adriatic surge of 21 June 1978 to mesoscale atmospheric forcing, *J. Geophys. Res.*, *115*, C06011, doi:10.1029/2009JC005777.

Orlić, M. (1980), About a possible occurrence of the Proudman resonance in the Adriatic, *Thalassia Jugoslavica*, *16*, 79–88.

Pasquet, S., and I. Vilibić (2013), Shelf edge reflection of atmospherically generated long ocean waves along the central U.S. East Coast, *Cont. Shelf Res.*, *66*, 1–8.

Pattiaratchi, C., and E. M. S. Wijeratne (2014), Observations of meteorological tsunamis along the south-west Australian coast, *Nat. Hazards*, *74*, 281–302, doi:10.1007/s11069-014-1263-8.

Pellikka, H., J. Rauhala, K. K. Kahma, T. Stipa, H. Boman, and A. Kangas (2014), Recent observations of meteotsunamis on the Finnish coast, *Nat. Hazards*, *74*(1), 197–215, doi:10.1007/s11069-014-1150-3.

Platzman, G. W. (1965), The prediction of surges in the southern basin of Lake Michigan: Part I. The dynamical basis for prediction, *Mon. Weather Rev.*, *93*(5), 275–281.

Pleim, J. E. (2007), A combined local and nonlocal closure model for the atmospheric boundary layer. Part I: Model description and test, *J. Appl. Meteorol. Climatol.*, *46*, 11,383–11,395.

Proudman, J. (1929), The effects on the sea of changes in atmospheric pressure, *Mon. Not. R. Astron. Soc. Geophys. Suppl.*, *2*(4), 197–209, doi:10.1111/j.1365-246X.1929.tb05408.x.

Rabinovich, A. B. (2009), Seiches and harbor oscillations, in *Handbook of Coastal and Ocean Engineering*, edited by Y. C. Kim, pp. 193–236, World Sci., Singapore.

Renault, L., G. Vizoso, A. Jansá, J. Wilkin, and J. Tintoré (2011), Toward the predictability of meteotsunamis in the Balearic Sea using regional nested atmosphere and ocean models, *Geophys. Res. Lett.*, *38*, L10601, doi:10.1029/2011GL047361.

Roberts, R. D., and J. W. Wilson (1989), A proposed microburst nowcasting procedure using single-Doppler radar, *J. Appl. Meteorol.*, *28*, 285–303, doi:10.1175/1520-0450(1989)028 < 0285:APMNPU>2.0.CO;2.

Schwab, D. J., and K. W. Bedford (1994), Initial implementation of the Great Lakes Coastal Forecasting System: A real-time system for predicting lake circulation and thermal structure, *Water Qual. Res. J.*, *29*(2–3), 203–220.

Schwab, D. J., G. A. Leshkevich, and G. C. Muhr (1992), Satellite measurements of surface water temperature in the Great Lakes: Great Lakes coastwatch, *J. Great Lakes Res.*, *18*(2), 247–258, doi:10.1016/S0380-1330(92)71292-1.

Schwab, D. J., G. A. Leshkevich, and G. C. Muhr (1999), Automated mapping of surface water temperature in the Great Lakes, *J. Great Lakes Res.*, *25*(3), 468–481, doi:10.1016/S0380-1330(99)70755-0.

Šepić, J., and A. B. Rabinovich (2014), Meteotsunami in the Great Lakes, Chesapeake Bay and on the Atlantic coast of the United States generated by the propagating "derecho" of 29–30 June 2012, *Nat. Hazards*, *74*, 75–107, doi:10.1007/s11069-014-1310-5.

Šepić, J., L. Denis, and I. Vilibić (2009), Real-time procedure for detection of a meteotsunami within an early tsunami warning system, *Phys. Chem. Earth*, *34*, 1023–1031, doi:10.1016/j.pce.2009.08.006.

Šepić, J. and I. Vilibić (2011), The development and implementation of a real-time meteotsunami warning network for the Adriatic Sea, *Natural Hazards and Earth System Sciences*, *11*(1), 83–91.

Šepić, J., I. Vilibić, and I. Fine (2015), Northern Adriatic meteorological tsunamis: Assessment of their potential through ocean modeling experiments, *J. Geophys. Res. Oceans*, *120*, 2993–3010, doi:10.1002/2015JC010795.

Skamarock, W. C., et al. (2008), A description of the advanced research WRF Version 3, *NCAR Tech. Note NCAR/TN-475+STR*, doi:10.5065/d68s4mvh, NCAR, Boulder, Colo.

Stumpf, G. J., A. Witt, E. DeWayne Mitchell, P. L. Spencer, J. T. Johnson, M. D. Eilts, K. W. Thomas, and D. W. Burgess (1998), The National Severe Storms Laboratory mesocyclone detection algorithm for the WSR-88D, *Weather Forecasting*, *13*, 304–326, doi:10.1175/1520-0434(1998)013 < 0304:TNSSLM>2.0.CO;2.

Tao, W. K., J. Simpson, and M. McCumber (1989), An ice-water saturation adjustment, *Mon. Weather Rev.*, *117*, 231–235.

Thiébaux, J., E. Rogers, W. Wang, and B. Katz (2003), A new high-resolution blended real-time global sea surface temperature analysis, *Bull. Am. Meteorol. Soc.*, *84*, 645–656.

Thomson, R. E., A. B. Rabinovich, I. V. Fine, D. C. Sinnott, A. McCarthy, N. A. S. Sutherland, and L. K. Neil (2009), Meteorological tsunamis on the coasts of British Columbia and Washington, *Phys. Chem. Earth*, *34*, 971–988, doi:10.1016/j.pce.2009.10.003.

Toledo Blade (1942), Freak Tidal Wave Sweeps Lake Erie Shoreline, Eight Believed Drowned.

Ursell, F. (1952), Edge waves on a sloping beach, *Proc. R. Soc. London, Ser. A*, *214*(1116), 79–98.

Vilibić, I. (2005), Numerical study of the Middle Adriatic coastal waters' sensitivity to the various air pressure travelling disturbances, *Ann. Geophys.*, *23*(12), 3569–3578, doi:10.5194/angeo-23-3569-2005.

Vilibić, I. (2008), Numerical simulations of the Proudman resonance, *Cont. Shelf Res.*, *28*(4–5), 574–581, doi:10.1016/j.csr.2007.11.005.

Vilibić, I., S. Monserrat, A. Rabinovich, and H. Mihanović (2008), Numerical modelling of the destructive meteotsunami of 15 June, 2006 on the coast of the Balearic Islands, *Pure Appl. Geophys.*, *165*(11–12), 2169–2195, doi:10.1007/s00024-008-0426-5.

Vilibić, I., K. Horvath, N. Strelec Mahović, S. Monserrat, M. Marcos, Á. Amores, and I. Fine (2014), Atmospheric processes responsible for generation of the 2008 Boothbay meteotsunami, *Nat. Hazards*, *74*, 25–53, doi:10.1007/s11069-013-0811-y.

Wertman, C. A., R. M. Yablonsky, Y. Shen, J. Merrill, C. R. Kincaid, and R. A. Pockalny (2013), Mesoscale convective system surface pressure anomalies responsible for meteotsunamis along the U.S. East Coast on June 13th, 2013, *Sci. Rep.*, *4*, 7143, doi:10.1038/srep07143.